J Mater Sci (2010) 45:5323–5331
DOI 10.1007/s10853-010-4580-7

Work-hardening behaviour of a heat-treatable AA7108 aluminium alloy deformed to intermediate strains by compression

Ida Westermann · Odd Sture Hopperstad · Knut Marthinsen · Bjørn Holmedal

Received: 25 March 2010 / Accepted: 28 April 2010 / Published online: 11 May 2010

Abstract This work is an experimental study of ageing and work-hardening considering various heat treatments of an AA7108 aluminium alloy in the as-cast and homogenized condition. Specimens have been exposed first to a solution heat treatment and a then to a two-step age-hardening to obtain different tempers. These tempers have been tested in an upsetting test applying state-of-the-art cold lubrication allowing intermediate strains to be reached before the onset of barrelling. The measured work-hardening response has been analyzed by fitting an extended Voce equation to the experimental stress–strain curves. With increasing overageing the stage III part of the stress–strain curve shrinks, and for the most overaged condition studied here, the stress–strain curve has reached a linear stage IV already at a strain of about 0.3. Interestingly, the slope of the stage IV curve then is lower than commonly reported for Al alloys. The microstructure and texture of the deformed material have been further investigated for a selection of tempers, and their influence on the work-hardening behaviour has been discussed.

I. Westermann (✉) · O. S. Hopperstad
Structural Impact Laboratory (SIMLab)–Centre for Research-Based Innovation and Department of Structural Engineering, Norwegian University of Science and Technology, 7491 Trondheim, Norway
e-mail: ida.westermann@ntnu.no

K. Marthinsen · B. Holmedal
Department of Materials Science and Engineering, Norwegian University of Science and Technology, 7491 Trondheim, Norway

Introduction

The combination of high-specific strength and ductility makes aluminium an exceptional material for energy absorption, and the high-strength aluminium alloys are therefore well suitable in car bumper systems designed to absorb energy in a collision. The 7*xxx* alloying systems belong to the heat-treatable alloys which owe their strength to the combination of work-hardening, precipitation-hardening and alloying elements in solid solution. The mechanical properties of these alloys are strongly dependent on the thermo-mechanical process and it is therefore important to understand the relationship between the microstructure evolution during thermo-mechanical processing and the mechanical properties.

Modelling a complex problem like work-hardening of heat-treatable alloys is not trivial. In the heat-treatable 7*xxx* aluminium alloying system, several mechanisms influence the work-hardening behaviour of the alloys, e.g. particle size and distribution, dislocation density and alloying elements in solid solution. The work-hardening mechanism is not only controlled by interactions between dislocations but also by the interaction between dislocations and precipitates. Hence, the strength, size and distribution of the precipitates are of great importance.

Several microstructure based work-hardening models have been proposed for predicting the mechanical properties. A one-parameter model, the mechanical threshold strength (MTS) model, was introduced by Kocks in 1976 [1], a model that has been further refined by Mecking and Kocks [2] and Estrin and Mecking [3]. This model only takes the overall dislocation density of the material into account. Other work-hardening models, which include more refined microstructure descriptions, have later been introduced and used by other authors, see e.g. [4–7].

A semi-empirical model based on the one-parameter MTS framework has been proposed by Cheng et al. [8] for prediction of the influence of the precipitate state on the work-hardening. In a previous study to this work [9], tensile data of different tempers of an as-cast and homogenized AA7108 aluminium alloy was fitted to an extended Voce equation applying two Voce terms to describe the plastic region up to the limited strains relevant for tensile tests. The fitted parameters were then analyzed in elucidation of the approach put forward by Cheng et al. An interesting finding in [9] was a very distinct region in the early plastic regime of the stress–strain curve, which was described by the extra term added to the extended Voce equation. It was suggested that heterogeneous flow, influenced by the precipitate distribution, gave rise to the necessity of this extra term. The other classical Voce term is dominating at higher strains and stresses, and is in agreement with what is expected for a typical stage III work-hardening behaviour [10].

As pointed out by Kocks and Mecking [10], the classical Voce equation [11] only gives a good description of hardening in the middle of stage III. Hockett and Sherby [12] applied the Voce equation as a phenomenological model to describe stress–strain curves. They used a slightly modified one-term version of the Voce equation to be able to describe the behaviour at larger strains than those obtained in tensile tests. Later, Follansbee and Kocks [13] generalized the MTS model making it capable of predicting realistic stress–strain curves at larger strains, using a one-parameter model with a microstructure anchorage.

As suggested by Sevillano et al. [14], the use of several terms in the hardening equation will give a better description of the entire curve at large strains. Hence, the extended Voce equation with several terms is suitable not only for describing tensile data but also deformation to larger strains like in compression tests. The presence and causes of a stage IV work-hardening were widely discussed in the 1970s and 1980s, see e.g. [12, 14–16], and is now a well-accepted work-hardening phenomenon, but the underlying mechanisms are far from fully understood [10, 17]. Stage IV work-hardening is characterized by a linear increase in the flow stress at large strains, i.e. the decreasing work-hardening rate in stage III starts to level out and becomes constant [16].

The aim of this work is to study work-hardening at larger strains in a commercial AA7108 aluminium alloy heat treated to different tempers and deformed by compression testing. The work is a continuation of the work on tensile testing presented in [9], and the data here are evaluated in the same way, in elucidation of the work-hardening model by Cheng et al. [8]. This model is based on the simple one-parameter representation of the dislocation density by Mecking and Kocks [2].

Material and experimental procedure

The experimental work was carried out on a commercial AA7108 aluminium alloy provided by Hydro Aluminium Structures Raufoss AS. This is an alloy used for extruded profiles for automotive applications. To rule out texture effects caused by the forming process, the experimental work was carried out on as-cast and homogenized ingot material with a random texture and an equiaxed grain-structure, see Fig. 1. Cylindrical compression specimens with a diameter of 10 mm and a height of 15 mm were machined from the centre region of the ingot. The specimens were all first subjected to a solid solution heat treatment at 480 °C for 20 min and stored at room temperature for 24 h. Subsequently, the specimens were subjected to a two-step artificial ageing, the first step being at 100 °C for 5 h followed by 150 °C for 3, 5, 9, 19, 50 and 268 h (11 days). To minimize friction between tool and specimen during compression testing, the specimens were industrially conversion coated after the heat treatment. The lubrication is a two-step process, which covers the material with a calcium aluminate inner layer and a sodium stearate top coating. Compression testing was carried out with a constant velocity of 2 mm/min, corresponding to a nominal strain rate of $2.2\ 10^{-3}\ s^{-1}$. The compression test was stopped when the 6 mm measure range of the extensometer was reached.

Specimens of the deformed 5 h and 268 h materials were prepared from the mid-section of the compressed samples for transmission electron microscopy (TEM) investigations by mechanical grinding and punching of 3 mm discs followed by electropolishing in a double-jet Tenupol by a 33% nitric acid solution in methanol operated at −20 °C and 15 V. The samples were investigated in a JEOL JEM-2010 TEM operated at a nominal voltage of 200 kV. In addition, the mid-sections of the two deformed alloys were investigated with respect to substructure in a

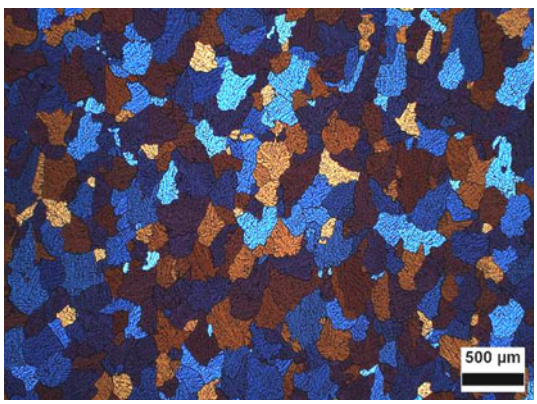

Fig. 1 Microstructure of the as-cast and homogenized material

field emission scanning electron microscope (FESEM) equipped with a Nordif CD200 EBSD-detector.

Results

The true stress, σ, and true strain, ε, were calculated from the compression tests, and the stress–strain curves are shown in Fig. 2. The plastic strain may then be found as $\varepsilon^{\mathrm{p}} = \varepsilon - \sigma/\sigma E$, where E is the Young's modulus. An extended Voce equation was then fitted to the experimental hardening curve, using a least-squares algorithm, in the range between $\varepsilon^{\mathrm{p}} = 0.002$ and till the test is stopped

$$\sigma = \sigma_0 + \sum_{i=1}^{n} \sigma_{si}\left(1 - \exp\left(-\frac{\theta_i}{\sigma_{si}} \cdot \varepsilon^{\mathrm{p}}\right)\right) \quad (1)$$

where σ_0 is a yield stress, and σ_{si} and θ_i are the saturation stress and the initial work-hardening rate for term i, respectively. The fitted σ_0 is a back-extrapolated stress at zero plastic strain. Based on Eq. 1 the work-hardening rate, θ, can be calculated as a function of the plastic strain as

$$\theta = \frac{\mathrm{d}\sigma}{\mathrm{d}\varepsilon^{\mathrm{p}}} = \sum_{i=1}^{n} \theta_i \exp\left(-\frac{\theta_i}{\sigma_{si}} \cdot \varepsilon^{\mathrm{p}}\right) \quad (2)$$

It is underlined that we use the extended Voce model here as a convenient representation of the experimental data.

For the tempers 3 to 19 h, three terms give a satisfactory fit to the experimental data. For the 50 h and 268 h tempers, only two terms are required. An expansion including three terms will be applied here in this work. The fitted stress–strain curve is assumed to be monotonically increasing and to avoid ambiguities the expansion terms are indexed so that $\theta_1 > \theta_2 > \theta_3$. For the curves only using two terms the first term is excluded (formally by $\sigma_{s1} \to 0$). In the extended Voce fitting, Eq. 1, the exponential decay

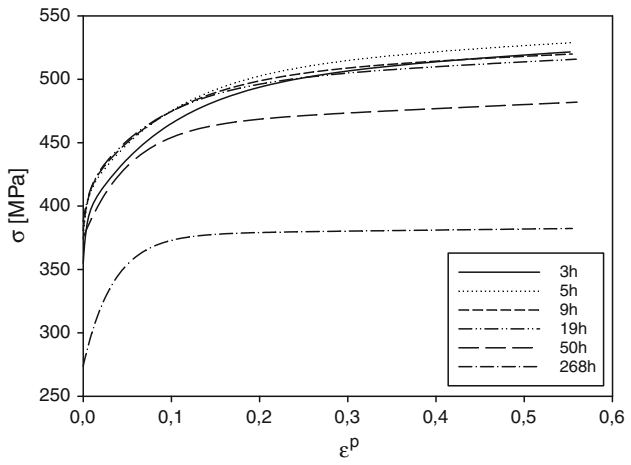

Fig. 2 The compressive true stress–strain curves plotted for the different tempers

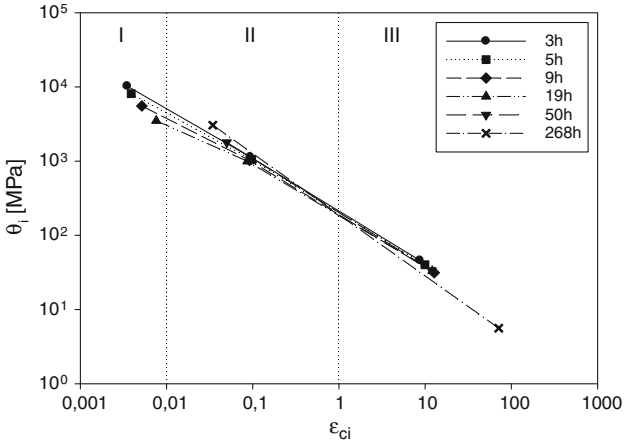

Fig. 3 Typical θ_i values for the three Voce terms plotted as a function of the characteristic strain for the different tempers. The *vertical lines* indicate characteristic strain values separating relevant strain ranges for the different Voce terms

of each of the involved Voce terms $\sigma_{si}(1 - \exp(-\varepsilon^{\mathrm{p}}/\varepsilon_{ci}))$ will make them saturate towards their saturation stresses σ_{si}. The strain scales for saturation to occur are given by the characteristic strains, $\varepsilon_{ci} = \sigma_{si}/\theta_i$. In Fig. 3, the θ_i values have been plotted with respect to their respective ε_{ci}. The three involved Voce terms have been categorized accordingly into three regions, as indicated in Fig. 3. It transpires from the figure that the work-hardening rates and strain scales of the two Voce terms used for the 50 and 268 h tempers correspond to the second and third terms for the other tempers. The third Voce term influences the shape of the stress–strain curve at the largest strains, and the final saturation stress is reached when this term approaches σ_{s3}. This occurs at a stress far beyond what is measured in the compression tests, where a linear stage IV work-hardening behaviour was exhibited for all tempers. To obtain linearity at the highest strains measured, the value of the saturation stress for the third Voce term, σ_{s3}, was chosen equal to 400 MPa for all the tempers.

Figure 4 illustrates how the work-hardening rate changes with increasing plastic strain. The tempers with three Voce terms (3–19 h) have a characteristic dramatic drop in work-hardening rate at low strains. At intermediate strains (<0.5) the decrease is less steep, and at strains larger than 0.5 the work-hardening rate becomes more or less constant. For the tempers with only two terms, the work-hardening rate becomes constant at strains around 0.3. Figure 5 shows the ageing curve at $T = 150$ °C for the considered alloy in terms of the compressive yield stress $R_{\mathrm{p0.2}}$ and the back-extrapolated σ_0 as a function of ageing time. The peak stress is reached after 9 h of ageing. The difference between the two values is largest for the underaged conditions compared to the peak- and over-aged tempers where the two values are more or less equal. It should

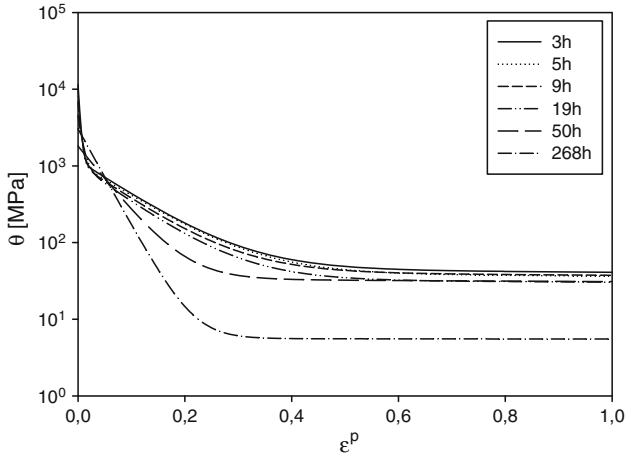

Fig. 4 The work-hardening rate based on the extended Voce rule plotted as a function of the plastic strain. The tempers 3–19 h are fitted with three terms, showing three distinct regions in the plot. The 50 and 268 h tempers are fitted with two terms

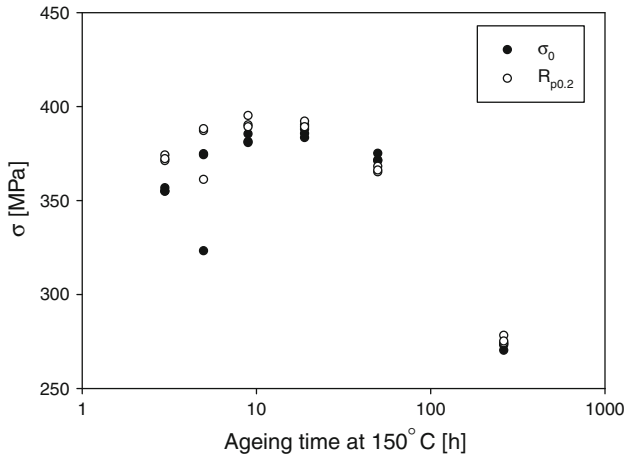

Fig. 5 The compressive yield stress for the alloy. Both the experimental $R_{p0.2}$ and the back-extrapolated σ_0 are shown

therefore be stated that σ_0 does not correspond to the yield stress in any direct sense.

The parameters in the three Voce terms may then be considered separately. The first Voce term is represented in Figs. 6a and 7a, which show the saturation stress, σ_{s1}, and initial work-hardening rate, θ_1, respectively, for the tempers 3–19 h. The saturation stress for the first Voce term, Fig. 6a, is low in value and decreases slightly with increasing ageing time. The initial work-hardening rate for the first Voce term, Fig. 7a, is in the order of 5.000–15.000 MPa, and is decreasing with increasing ageing time, i.e. the first Voce term saturates quickly in agreement with the observation in Fig. 3. One exception is the 5 h temper where one of the three observations shows both a much higher saturation stress as well as initial work-hardening rate. The relevant strain scale, $\varepsilon_{c1} = \sigma_{s1}/\theta_1$, for this initial region is in the order of 0.004, see Fig. 3. The saturation stress for the second Voce term, Fig. 6b, is higher than the first saturation stress. It decreases from ~105 MPa at 3 h to ~85 MPa at 19 h and then it increases again for the overaged conditions. The initial work-hardening rate for the second Voce term, Fig. 7b, is more or less constant around 1,000 MPa for the tempers 3–19 h, it then increases for the overaged samples to around 3,000 MPa for the 268 h temper.

Since the saturation stress, σ_{s3}, is kept constant at 400 MPa for the third Voce term, only the initial work-hardening rate, θ_3, shown in Fig. 7c, is varying. In general, the initial work-hardening rate is very low for the third Voce term compared to the other two terms. For the 3 h temper it is slightly higher, ~50 MPa, than for the tempers 5–50 h where it is around ~35 MPa. For the overaged 268 h temper, the initial work-hardening rate has decreased to around 5 MPa.

The tempers 5 and 268 h were chosen for further investigation of the microstructure. The micrographs in Fig. 8 show the mid-sections of the deformed samples. Despite the coating applied to avoid friction between the sample and the test rig during testing, some early barrelling is still observed at a strain of 0.55. Both tempers show heterogeneous deformation in the form of conical shear deformation zones indicated by dashed lines, which seems more dominant in the 268 h temper. The contact surfaces at the top and bottom of the samples show little deformation compared to the centre regions.

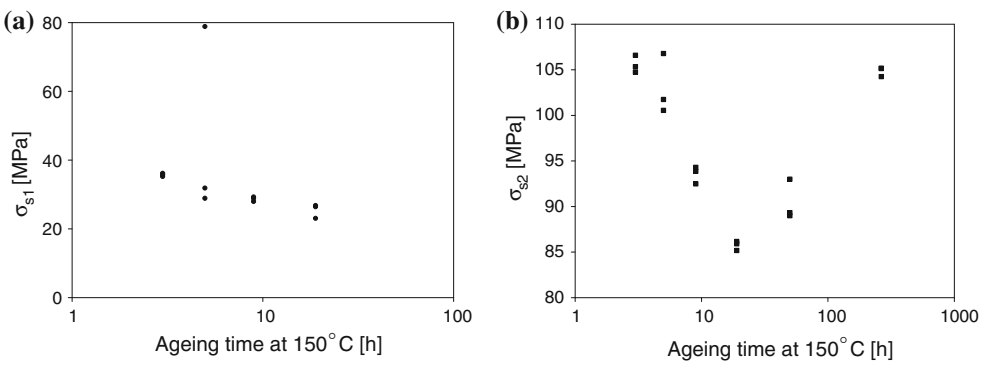

Fig. 6 The saturation stresses, σ_{si}, plotted as a function of the ageing time: **a** the first Voce term and **b** the second Voce term

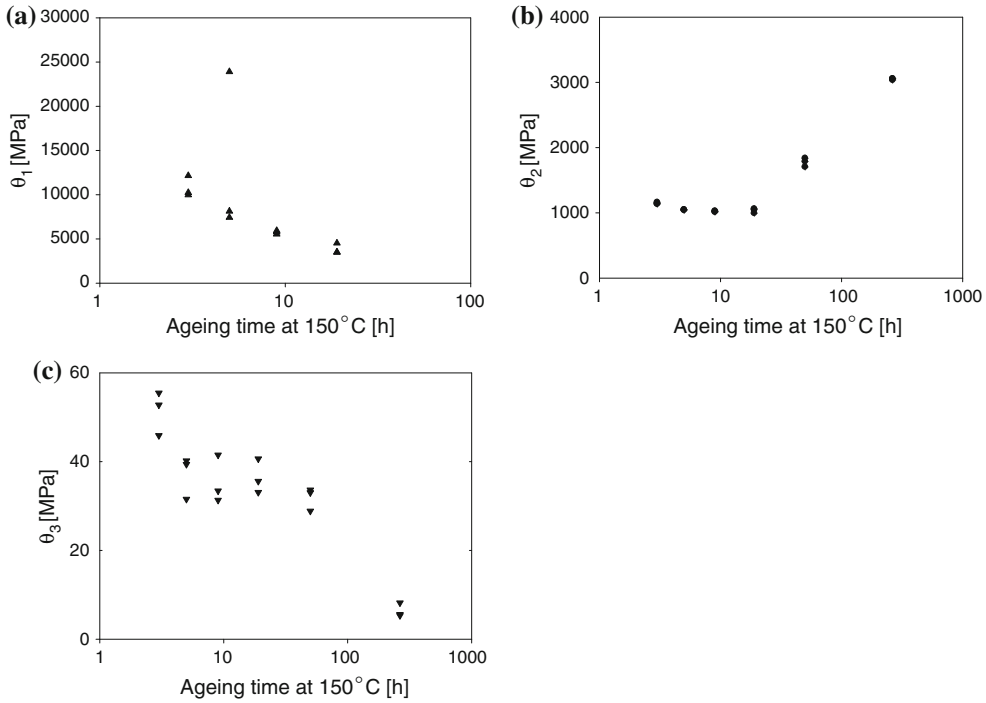

Fig. 7 The initial work-hardening rates for the different Voce terms plotted as a function of ageing time: **a** the first Voce term, **b** the second Voce term and **c** the third Voce term

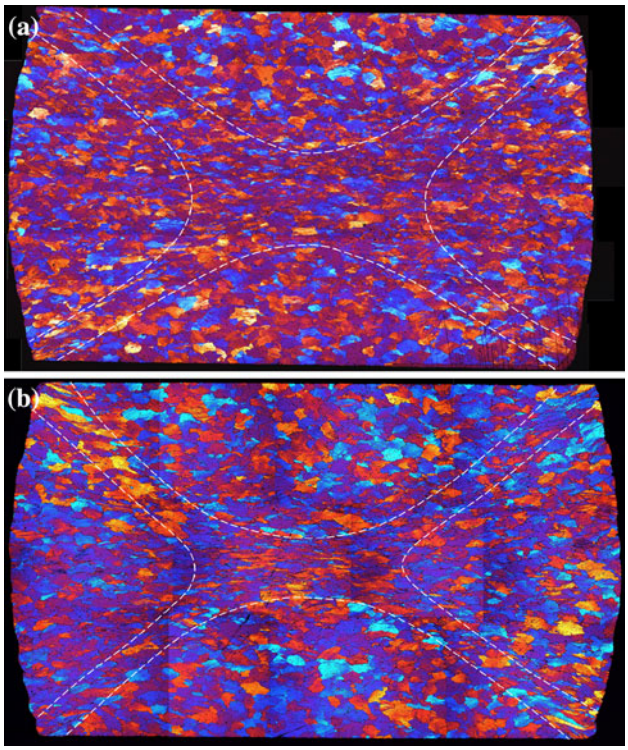

Fig. 8 Mid-section of the compressed samples showing the heterogeneous microstructure and barrelling caused by the compression test **a** 5 h temper and **b** 268 h temper

TEM samples were prepared from the centre region of the deformed 5 and 268 h samples and the microstructures are seen in Fig. 9. The precipitates in the 5 h material are spherical and the size range is ~5 nm, Fig. 9a. It is not possible to determine whether the precipitates have been sheared by dislocations or not. Figure 9b shows the deformed 268 h material. The precipitates in this material are much larger and spherical to ellipsoidal in shape and in the size range from 5 to 25 nm. Despite the deformation it is not possible to determine from these TEM images if the precipitates have been sheared or by-passed by the dislocations.

The orientation imaging map in Fig. 10 is collected in the SEM using the EBSD technique. The figure illustrates one quarter of the cross-section of the deformed 5 h sample and the shear-zone caused by the barrelling is clearly seen here at a strain of 0.55. Micro shear-bands are observed within some of the individual grains. The corresponding texture of this deformed 5 h sample was determined and is represented as pole figures in Fig. 11 showing a weak ⟨110⟩-fibre texture as expected for fcc uniaxial compression tests. The orientation imaging map in Fig. 12 shows an example of an interior grain in the deformed 268 h material. Due to the deformation, subgrains within the grains might be expected, and therefore this EBSD scan was made with a small step size in an attempt to determine

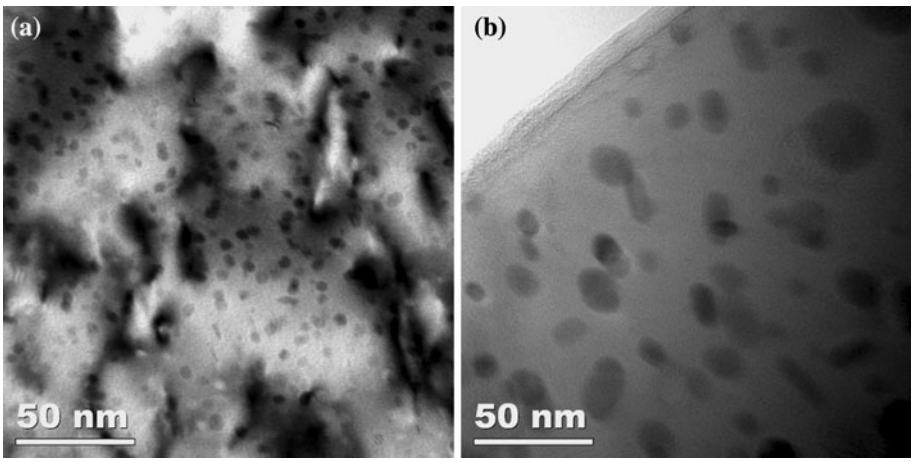

Fig. 9 TEM bright field image of the deformed material **a** 5 h temper and **b** 268 h temper

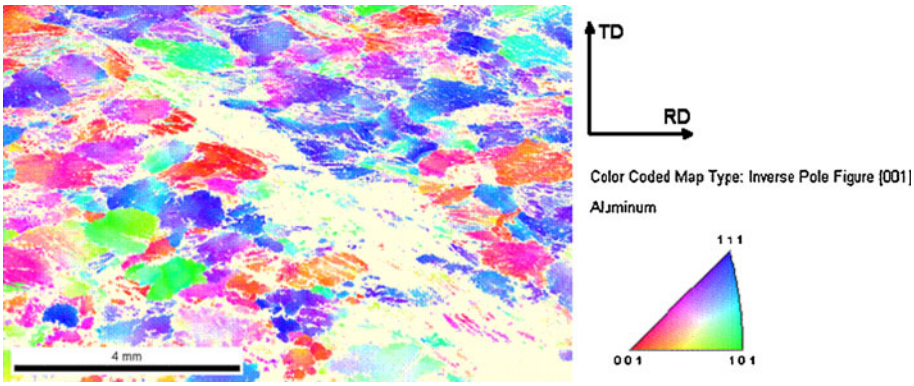

Fig. 10 EBSD map from the lower right corner of the compressed 5 h sample in Fig. 8a. The *white areas* are a result of the combination of a big step size (20 μm) as well as poor indexing in the heavily deformed shear-zone

subgrains. The grain does, however, not contain any distinguishable subgrains, but local rotation gradients are observed as weak colour gradients within the grain. The white spots are most likely due to second-phase particles which have not been indexed.

Discussion

A comparison of the different Voce terms obtained in the compression tests of this work to the earlier work on tensile tests [9] reveals the same trend. At the onset of yielding, the work-hardening rate is very high in both cases. A possible explanation is heterogeneous flow caused by the precipitate distribution in the material. This phenomenon was discussed in [9] and will not be further emphasized in this study. For the tensile data in [9], the second Voce term gives a good description of the early stage III work-hardening up to necking at strains of 0.06–0.07, whereas a larger range of strain is fitted for the compression data. For the underaged conditions the saturation stress, σ_{s2}, is generally larger in tension than in compression, but the trend is similar, where σ_{s2} decreases with increasing ageing time. For the overaged conditions on the other hand, σ_{s2} increases with increasing ageing time for the compression test, whereas it remains approximately constant in tension. Both cases have a distinct change of ageing time dependency between underaged and overaged conditions. According to Cheng et al. [8], the parameter that determines the transition between shearable and non-shearable precipitates is a distinct change in the ageing time dependency of $d\theta/d\sigma$, i.e. the derivative of the work-hardening rate with respect to the flow stress. Since the first Voce term saturates at small strains and the contribution to $d\theta/d\sigma$ from the third Voce term is negligible, $d\theta/d\sigma$ simply becomes (cf. Eq. 2):

$$\frac{d\theta}{d\sigma} = -\frac{\theta_2}{\sigma_{s2}} \tag{3}$$

The magnitude of this parameter is plotted against the ageing time in Fig. 13. The same trends are observed for the compression data as was observed for the tension data. In both cases this transition occurs somewhere between 9 and 19 h of ageing, i.e. according to this theory the shearable/non-shearable transition occurs close to peak strength in the slightly overaged temper. This is also what Cheng et al. [8] have observed for both an AA6111 aluminium

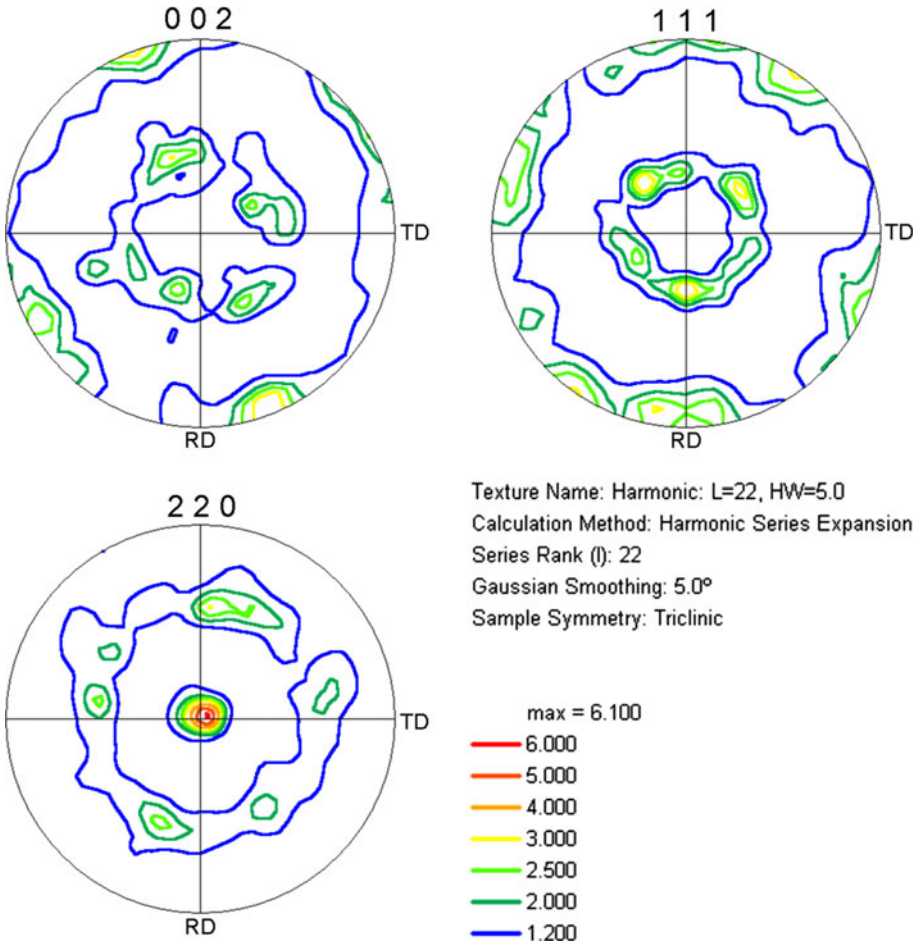

Fig. 11 The 002-, 111- and 220-pole figures based on the orientation imaging map in Fig. 10 of the deformed 5 h temper showing a weak ⟨110⟩-fibre

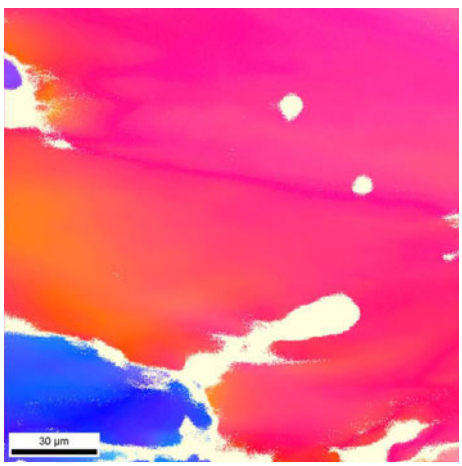

Fig. 12 Orientation imaging map of the 268 h temper from the interior of the sample

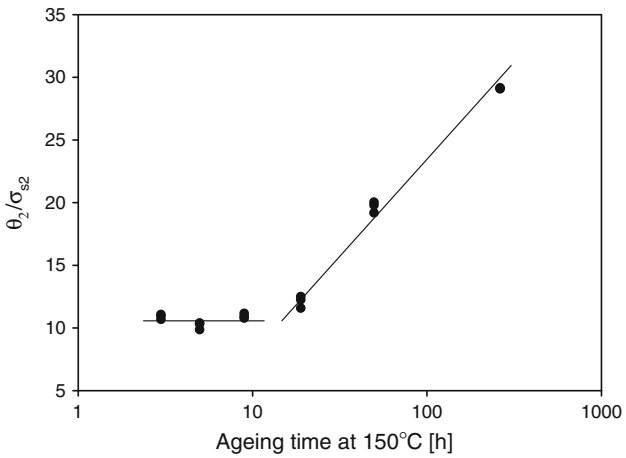

Fig. 13 The parameter θ_2/σ_{s2} plotted for the different tempers. Lines have been added just to indicate the trend

alloy and an AA7030 alloy. Deschamps and Brechet [18] and Poole et al. [19] assume that this transition occurs around peak strength when modelling precipitation-hardening. Cheng et al. [8] argue that the parameter $d\theta/d\sigma$ can be interpreted as a direct measure of the rate of dynamic recovery. Thus, when the precipitates are shearable, this parameter remains more or less constant. Whereas the shearable/non-shearable transition has been observed by detailed TEM investigations and reported for the 6*xxx* series [20], it has not been possible to find any literature on

such experimental findings for the 7*xxx* series. The spherical and ellipsoidal shapes of the particles in the 7*xxx* series, Fig. 9, are not optimal for observing shearing or breakage compared to the needle- and lath-shaped particles in the 6*xxx* alloys.

Regarding the third Voce term, one may argue whether it is appropriate to handle this term by keeping the saturation stress, σ_{s3}, constant. As can be seen from Fig. 4, the result is that the third Voce term is forced to give an approximately linear work-hardening rate in accordance with what is expected for typical stage IV behaviour. However, this third term gives the opportunity to include the much discussed appearance of a stage V work-hardening [21–24], i.e. when passing the characteristic strain, $\varepsilon_{c3} = \sigma_{s3}/\theta_3$, and approaching the saturation stress, the material experiences stage V work-hardening. By keeping the saturation stress constant at a high value (in this case 400 MPa), the characteristic strain, ε_{c3}, is in the order of 10 for the underaged tempers as shown in Fig. 3. This implies that as the compression test is stopped at a strain of about 0.5, the stress contribution from the third term is small. To be able to estimate the saturation stress of the third Voce term more accurately, experimental studies to larger strains should be carried out. Since the saturation stress σ_{s3} was prescribed at this large level, the initial work-hardening rate θ_3 is efficiently a freely varying parameter that can be chosen for fitting the largest strains measured in the compression tests.

In a study with varying amount of Mg in solid solution and its influence on work-hardening behaviour, Ryen et al. [25] have reported that at large strains the stage IV work-hardening rate becomes constant with a value of ca. 30 MPa independent of Mg content. What is observed in Fig. 7c is that for the underaged tempers, where shearable particles are expected, the work-hardening rate is found to be more or less constant around 35 MPa independent of ageing time. It is noted that Ryen et al. [25] obtained large strains by the combination of rolling and tension. In these tests, the influence of friction is avoided, but instead a strain path change is involved.

Despite the lubrication used in the compression tests, we still observe barrelling in Fig. 8 at a strain of 0.55. Due to the friction, an over-estimation of the work-hardening rate in stage IV would be expected. The influence of barrelling, as observed for the 5 h temper in Fig. 8a, is more complex to analyse but is believed to be weak at this early onset of localization. For the overaged samples, the initial work-hardening rate decreases, cf. Fig. 7c. The work-hardening rate for the 268 h temper almost disappears, as also observed from the stress–strain curve in Fig. 2, where the curve reaches a saturation stress already at a fairly small strain and is almost horizontal at strains larger than 0.3.

The deformed 268 h temper in Fig. 8b seems to be more prone to barrelling and shear-zone formation than the underaged 5 h temper in Fig. 8a. The orientation imaging map of interior grains in Fig. 12 reveals no subgrain boundaries (misorientations between 1° and 15°) within the grains and only some small local rotation gradients of the lattice, despite the large deformation. This indicates that the deformation is somewhat heterogeneous at this late stage of the test, with larger strains in the localized shear-zones than in the rest of the sample. The presence of large non-shearable precipitates and a depleted matrix for the overaged sample seem to enhance the tendency to shear-zone formation. While friction is expected to increase the apparent work-hardening rate as barrelling occurs, the existence of shear-zones will have the opposite effect.

Seeger [26] suggests that a change in the texture from random towards the ⟨110⟩-fibre texture can lead to a softening of the material, due to a lower inverse Schmid factor for this texture component. However, the Taylor model should be more applicable and a calculation of the evolution in Taylor factor during compression, to strains relevant for the present work (Fig. 14), indicates that this does not apply in our case. A full-constraint Taylor model was used for the calculation. It was found that the Taylor factor changes only to a small extent. It decreases slightly at first and then it increases with increasing strains. A similar evolution in Taylor factor has also been reported by Kopacz et al. [27] for a self-consistent model. Such a small change of the Taylor factor will not contribute much, and the increase in Taylor factor with increasing strains contributes only to a slightly increased work-hardening rate. The change in texture due to deformation should be similar for all the tempers; hence a similar change in Taylor factor is expected. This means that the texture evolution cannot explain the low work-hardening rate for the overaged 268 h condition. The explanation must lie in the interaction between dislocations, particles and alloying elements in

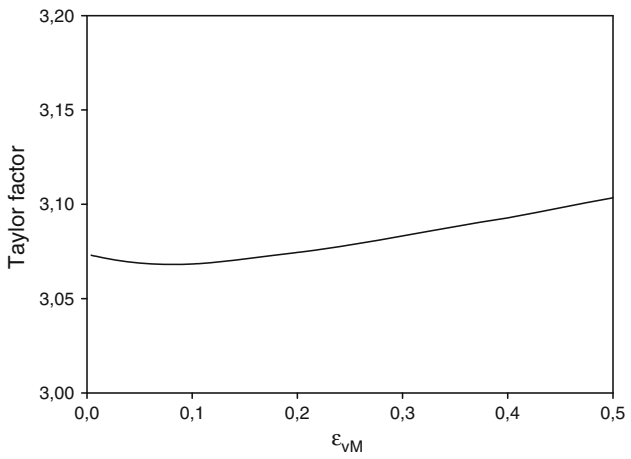

Fig. 14 The calculated evolution in Taylor factor when deforming a material with initial random texture by compression

solid solution. For the overaged conditions the matrix is depleted with respect to alloying elements and the precipitates are incoherent. This is similar as reported by Dumont et al. [28] who have observed that the initial work-hardening rate increases for two overaged 7*xxx* alloys due to accumulation of dislocations at non-shearable particles, whereas this effect is not observed at larger strains. Their results are in agreement with what is observed here, namely that θ_2 increases for the overaged conditions whereas θ_3 decreases.

Conclusion

It has been shown that the use of an extended Voce rule with several terms gives a good description of the compression test data up to intermediate strains. This allows us to analyse the hardening parameters at the different stages of work-hardening. For the underaged conditions a very high work-hardening rate is observed at the very beginning of the plastic regime, which is not seen for the overaged conditions.

In the region with stage III work-hardening, the initial work-hardening rate decreases with increased ageing time for the underaged conditions, whereas it increases for the overaged conditions. This transition occurs close to the peak age and is interpreted as a change in the precipitate nature from shearable to non-shearable.

At higher strains an early onset of stage IV work-hardening behaviour is observed with a more or less constant work-hardening rate. The slope of the stress strain curve is here independent of temper, except for the most overaged temper, 268 h. It is a very interesting finding that the work-hardening rate for the sample aged for 268 h almost disappears at larger strains. This observation is attributed to the interaction between dislocations and the non-shearable, incoherent precipitates in the overaged temper.

References

1. Kocks UF (1976) Trans ASME 98:76
2. Mecking H, Kocks UF (1981) Acta Metall 29:1865
3. Estrin Y, Mecking H (1984) Acta Metall 32:57
4. Mughrabi H (1987) Mater Sci Eng 85:15
5. Gottstein G et al (2000) Acta Mater 48:4181
6. Nes E, Marthinsen K (2002) Mater Sci Eng A 322:176
7. Friis J et al (2006) Mater Sci Forum 519–521:1901
8. Cheng LM et al (2003) Metall Mater Trans A 34A:2473
9. Westermann I et al (2009) Mater Sci Eng A 524:151
10. Kocks UF, Mecking H (2003) Prog Mater Sci 48:171
11. Voce E (1948) J Inst Met 74:537
12. Hockett JE, Sherby OD (1975) J Mech Phys Solids 23:87
13. Follansbee P, Kocks U (1988) Acta Metall 36:81
14. Sevillano JG et al (1981) Prog Mater Sci 25:69
15. Mecking H, Grinberg A (1975) In: 5th ICSMA, international conference on the strength of metals and alloys, p 298
16. Rollett AD et al (1987) In: Sachdev AK, Embury JD (eds) Formability and metallurgical structure. TMS, Warrendale, PA, USA
17. Pantleon W (2004) Mater Sci Eng A 387–389:257
18. Deschamps A, Bréchet Y (1999) Acta Mater 47:293
19. Poole WJ et al (2000) Metall Mater Trans A 31A:2327
20. Poole WJ et al (2005) Philos Mag 85:3113
21. Zehetbauer M, Seumer V (1993) Acta Metall Mater 41:577
22. Dalla Torre FH et al (2006) Acta Mater 54:1135
23. Mülders B et al (2002) Mater Sci Eng A 324:244
24. Nes E et al (2000) Scripta Mater 43:55
25. Ryen Ø et al (2006) Metall Mater Trans A 37A:2007
26. Seeger A (2001) Philos Mag Lett 81:129
27. Kopacz I et al (1999) Model Simul Mater Sci Eng 7:875
28. Dumont D et al (2004) Mater Sci Technol 20:567